Chapter 4

Multiple Source FMCW Reflectometry

4.1 Introduction

In this chapter we describe a novel approach aimed at increasing the effective bandwidth of a frequency-modulated continuous-wave (FMCW) ranging system. This is achieved by combining, or stitching, separate swept-frequency lasers (SFLs), to approximate a swept-source with an enhanced bandwidth [13, 14, 19]. The result is an improvement in the range resolution proportional to the increase in the swept-frequency range. This technique bears resemblance to synthetic aperture radar, in which radio frequency (RF) signals collected at multiple physical locations are used to approximate a large antenna aperture, and hence a high transverse resolution. In multiple source FMCW reflectometry, the synthesized aperture is not physical, but instead represents the accessible optical frequency range. This technique is of particular interest in the context of the SCL-based optoelectronic SFL. MS-FMCW leverages narrow SCL linewidths to present a pathway towards long-distance ranging systems with sub-100 μm resolutions.

We start our discussion of MS-FMCW by generalizing the results of chapter 2 to the case of multiple sources. We consider software and hardware implementations of stitching—the action of synthesizing a high-resolution range measurement from multiple source data sets—and present a series of experiments that demonstrate the

MS-FMCW principle. The culmination of this effort is a four-VCSEL system capable of ranging with an effective optical bandwidth of 2 THz, and a corresponding free-space axial resolution of 75 μm.

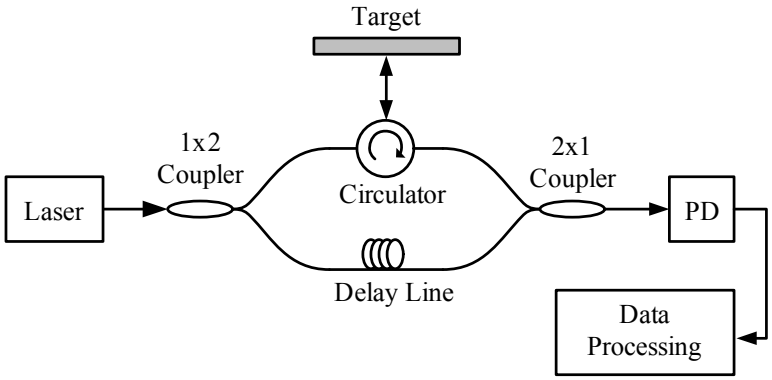

Figure 4.1: Schematic of an FMCW ranging experiment. PD: Photodetector

4.2 Theoretical Analysis

4.2.1 Review of FMCW Reflectometry

We begin our discussion with a brief review of FMCW reflectometry (see chapter 2 for a full discussion). Consider the FMCW ranging experiment shown in figure 4.1. The normalized electric field of the linearly chirped SFL is given by

$$e(t) = \text{rect}\left(\frac{t - T/2}{T}\right)\cos\left(\phi_0 + \omega_0 t + \frac{\xi t^2}{2}\right), \tag{4.1}$$

where T is the scan duration, ξ is the slope of the optical chirp, and ϕ_0 and ω_0 are the initial phase and frequency, respectively. The total frequency excursion is therefore given by $B = \xi T/2\pi$. For a single scatterer with round-trip delay τ and reflectivity R, the ω-domain photocurrent is given by

$$y(\omega) = \sqrt{R}\,\text{rect}\left(\frac{\omega - \omega_0 - \pi B}{2\pi B}\right)\cos\left(\omega\tau - \frac{\xi\tau^2}{2}\right). \tag{4.2}$$

The signal processing consists of calculating the Fourier transform (FT)[1] of $y(\omega)$ with respect to the variable ω, which yields a sinc peak centered at the delay τ.

$$Y(\zeta) = \pi B\sqrt{R}\,\exp\left(-j\frac{\xi\tau^2}{2}\right)\exp\left[-j(\zeta-\tau)(\omega_0+\pi B)\right]\mathrm{sinc}\left[\pi B(\zeta-\tau)\right], \qquad (4.3)$$

where ζ is the independent variable of the FT of $y(\omega)$, and has units of time. $Y(\zeta-\tau)$ is therefore the axial point spread function (PSF) of the FMCW system.

The range resolution is given by the location of the first null of the sinc function in equation (4.3) [37, 39]. This happens at $\zeta = \tau + 1/B$, which corresponds to a free-space range resolution

$$\Delta d = \frac{c}{2B}, \qquad (4.4)$$

where c is the speed of light. An equivalent metric of the resolution of the FMCW system is the full width at half maximum (FWHM) of the sinc function, given by

$$\mathrm{FWHM} \approx \frac{3.79}{\pi B} = \Delta d\frac{7.58}{\pi c} \qquad (4.5)$$

Let us now consider the following view of an FMCW imaging system. The target is characterized by some underlying function of the optical frequency, $y_{\mathrm{target}}(\omega)$, given by

$$y_{\mathrm{target}}(\omega) = \sum_n \sqrt{R_n}\cos\left(\omega\tau_n - \frac{\xi\tau_n^2}{2}\right), \qquad (4.6)$$

where τ_n and R_n are the delays and reflectivities of the multiple reflectors that make up the target. In deriving equation (4.6) we have assumed highly transparent reflectors ($R_n \ll 1$), and ignored interference between reflected beams. The FMCW photocurrent is then given by

$$y(\omega) = a(\omega)y_{\mathrm{target}}(\omega), \qquad (4.7)$$

where $a(\omega)$ is the rectangular window function, as in equation (4.2). The function

[1] In the following analysis we use capital letters to denote the FTs of the corresponding lower-case functions.

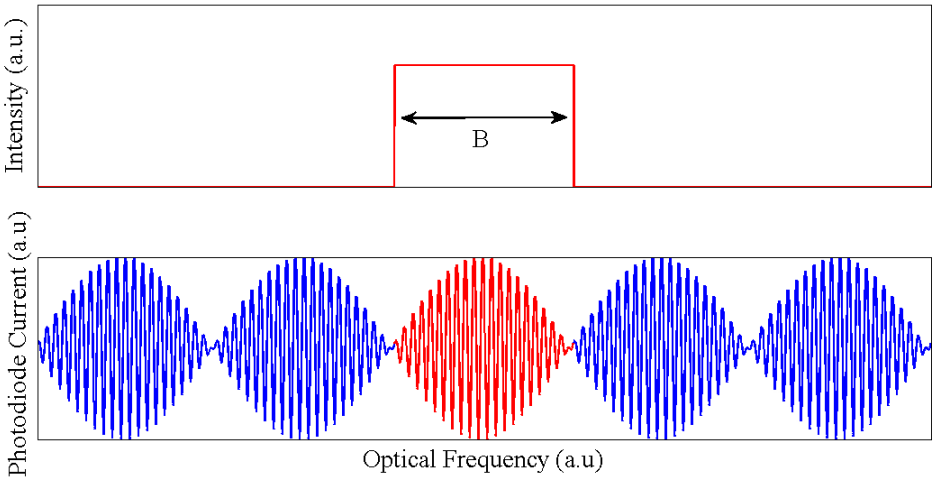

Figure 4.2: Schematic representation of single-source FMCW reflectometry. Top panel: the window function $a(\omega)$ corresponding to a single chirp. Bottom panel: The underlying target function $y_{\text{target}}(\omega)$ (blue) and its portion that is measured during the single sweep (red)

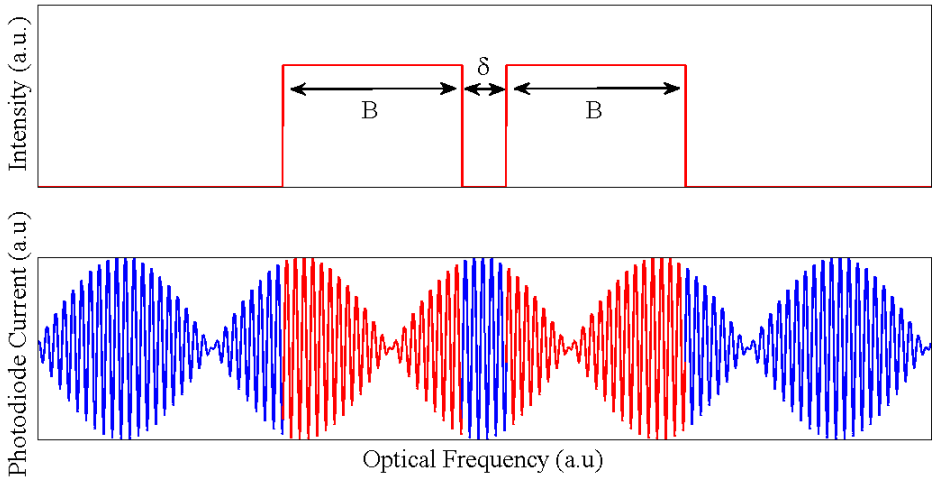

Figure 4.3: Schematic representation of dual-source FMCW reflectometry. Top panel: the window function $a(\omega)$ corresponding to two non-overlapping chirps. Bottom panel: The underlying target function $y_{\text{target}}(\omega)$ (blue) and its portion that is measured during the two sweeps (red)

$y_{\text{target}}(\omega)$ contains all the information about the target, and perfect resolution is obtained if $y_{\text{target}}(\omega)$ is known for all values of the optical frequency ω. The measurement in equation (4.7) gives us partial information about $y_{\text{target}}(\omega)$, collected over the frequency excursion defined by $a(\omega)$, resulting in a nonzero Δd. This single-source measurement is illustrated in figure 4.2.

We next develop the theory of MS-FMCW reflectometry, in which multiple sources sweep over distinct regions of the optical spectrum. The motivation for this approach is that the use of multiple sources allows us to further characterize $y_{\text{target}}(\omega)$. Figure 4.3 shows a schematic representation of a dual-source FMCW measurement. The target information is collected over a larger portion of the optical spectrum, resulting in an increase in the effective B, and a corresponding decrease in Δd.

4.2.2 Multiple Source Analysis

Taking the FT of equation (4.7), and equation (4.6), we arrive at the expression

$$Y(\zeta) = \frac{1}{2}\sum_n \sqrt{R_n}\exp\left(-j\frac{\xi\tau_n^2}{2}\right)A(\zeta-\tau_n), \tag{4.8}$$

which has peaks at $\zeta = \tau_n$. The axial PSF (i.e., the shape of the peaks) is given by the FT $A(\zeta)$ of the window function $a(\omega)$. We model the use of multiple sources with a window function $a_N(\omega)$ that comprises N non-overlapping rectangular sections, as shown in the top panel of figure 4.4a. The approach is easily modified to include overlapping sections. The k-th sweep originates at $\omega_{0,\,k}$, and is characterized by an angular frequency excursion $2\pi B_k$, where $k = 1, \ldots, N$. As illustrated in the middle and bottom panels of figure 4.4a, $a_N(\omega)$ can be decomposed into a rectangular window with width $2\pi\tilde{B} \equiv 2\pi\left[\sum_{k=1}^{N} B_k + \sum_{k=1}^{N-1}\delta_k\right]$, and a set of thin rectangular sections (gaps). Each gap represents the frequency range $2\pi\delta_k$ between the end of the k-th sweep and the beginning of the (k+1)-th sweep, across which no photocurrent is measured. Amplitudes of the ζ-domain FTs of the functions in figure 4.4a are shown in figure 4.4b. We observe that if the gaps are chosen sufficiently small, their effect in the ζ-domain can be treated as a small perturbation of the single sweep of

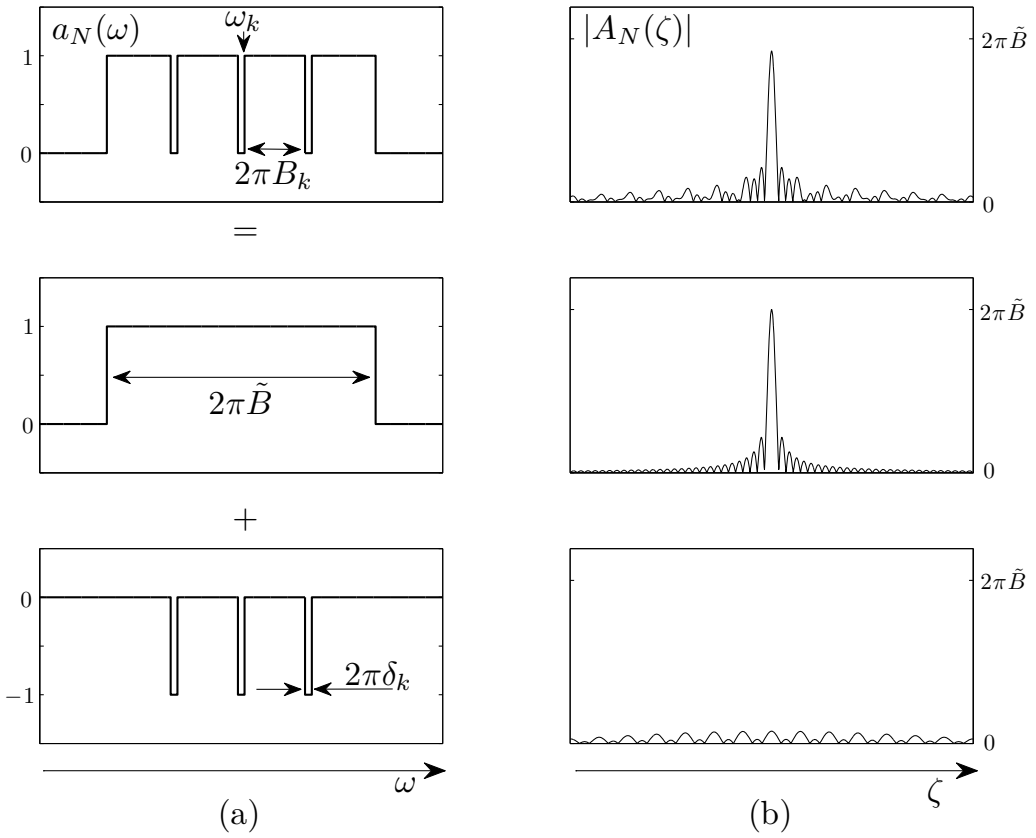

Figure 4.4: Multiple source model. (a)ω-domain description. The top panel shows a multiple source window function $a_N(\omega)$. This function may be decomposed into the sum of a single-source window function (middle panel) and a function that describes the inter-sweep gaps (bottom panel). (b)ζ-domain description. The three figures show the amplitudes of the ζ-domain FTs of the corresponding functions from part (a).

bandwidth $2\pi\tilde{B}$.

Therefore, an N-source sweep is described by

$$a_N(\omega) = \text{rect}\left(\frac{\omega - \omega_{0,1} - \pi\tilde{B}}{2\pi\tilde{B}}\right) - \sum_{k=1}^{N-1} \text{rect}\left(\frac{\omega - \omega_{0,\,k+1} + \pi\delta_k}{2\pi\delta_k}\right) \tag{4.9}$$

in the ω-domain, and by

$$\begin{aligned} A_N(\zeta) = {} & 2\pi\tilde{B}\exp\left[-j\zeta(\omega_{0,1} + \pi\tilde{B})\right]\text{sinc}\left(\zeta\tilde{B}\right) \\ & - 2\pi\sum_{k=1}^{N-1}\delta_k \exp\left[-j\zeta\left(\omega_{0,\,k+1} - \pi\delta_k\right)\right]\text{sinc}(\zeta\delta_k) \end{aligned} \tag{4.10}$$

in the ζ-domain. To find the range resolution we find the first null of equation (4.10). Expanding near $\zeta = 1/\tilde{B}$ and using the approximation $\sum_{k=1}^{N-1}\delta_k \ll \sum_{k=1}^{N} B_k$ yields

$$\zeta_{\text{null}}^{-1} = \left|\tilde{B}\exp\left[-j\zeta_{\text{null}}(\omega_{0,1} + \pi\tilde{B})\right] + \sum_{k=1}^{N-1}\delta_k\exp\left[-j\zeta_{\text{null}}\left(\omega_{0,k+1} - \pi\delta_k\right)\right]\right|. \tag{4.11}$$

Equation (4.11) can be solved numerically to find ζ_{null}. We note that an upper bound on ζ_{null}, and consequently on the range resolution, may be obtained by applying the triangle inequality to equation (4.11), to yield

$$\Delta d_{\text{MS-FMCW}} \leq \frac{c}{2\sum_{k=1}^{N} B_k}. \tag{4.12}$$

The conclusion is that by sweeping over distinct regions of the optical spectrum, we collect enough information about the target to arrive at an range resolution equivalent to the total traversed optical bandwidth, provided that the said bandwidth is much greater than the inter-sweep gaps.

4.2.3 Stitching

We next consider the problem of stitching, that is, synthesizing a measurement with enhanced resolution using photocurrents collected from multiple sweeps. In the pre-

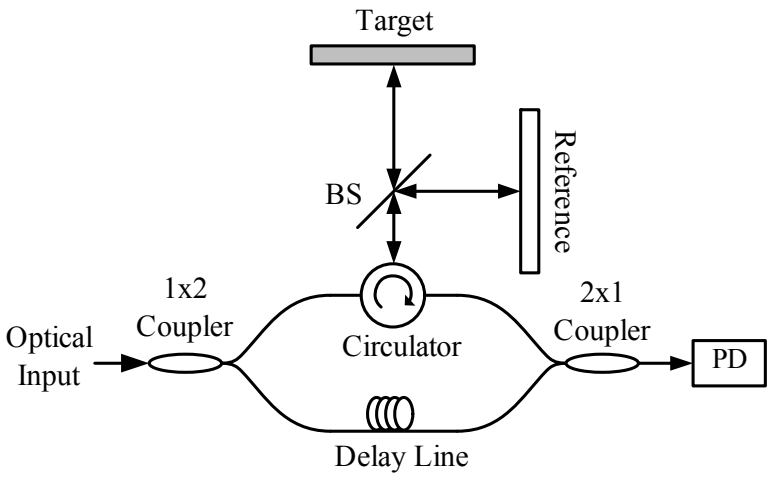

Figure 4.5: Schematic of a multiple source FMCW ranging experiment. A reference target is imaged along with the target of interest, so that the inter-sweep gaps may be recovered. BS: Beamsplitter. PD: Photodetector

ceding sections we have mapped photocurrents from the time domain to the optical frequency domain. Since the optical frequency is linear in time, this mapping involves first scaling the time axis by the chirp slope, and then translating the data to the correct initial frequency. Whereas the rate of each chirp is precisely controlled [1], the starting sweep frequencies are not known with sufficient accuracy. To reflect this uncertainty, we omit the translation step, so that the data collected during the k-th scan is given by

$$y_k(\omega) = \text{rect}\left(\frac{\omega - \pi B_k}{2\pi B_k}\right) y_{\text{target}}(\omega + \omega_{0,k}). \tag{4.13}$$

The stitched measurement, given by $y_{\text{stitched}} = a_N(\omega) y_{\text{target}}(\omega)$, can be written in terms of functions $y_k(\omega)$ using equation (4.9):

$$y_{\text{stitched}}(\omega) = \sum_{k=1}^{N} y_k(\omega - \omega_{0,k}). \tag{4.14}$$

The magnitude of the FT of equation (4.14) may be used for target recognition, and is given by

$$|Y_{\text{stitched}}(\zeta)| = \left| \sum_{k=1}^{N} \exp\left[-j2\pi\zeta \sum_{l=1}^{k-1} (B_l + \delta_l)\right] Y_k(\zeta) \right|. \tag{4.15}$$

The uncertainty in the starting frequencies manifests itself as an uncertainty in the inter-sweep gaps. To recover the gaps, we use a known reference target along with the target of interest, as shown in figure 4.5. By analyzing the data collected from the reference target, we are able to extract the parameters δ_k, and stitch together the target of interest measurement, according to equation (4.15).

To develop a gap recovery algorithm, we examine a two-sweep system with a single gap δ. The case of more than two sources may then be treated by applying this algorithm to adjacent sweeps in a pairwise manner. For simplicity we consider sweeps of equal slopes ξ, durations T, and therefore, bandwidths B. Suppose the known reference target consists of a single reflector with reflectivity R_a, located at the delay τ_a. The experiment of figure 4.5 generates two photocurrents, one for each sweep, of the form of equation (4.2). The initial photocurrent phase depends on the starting frequency of the corresponding sweep, and will change as the inter-sweep gap varies. Therefore, by considering the phase difference between the two photocurrents, we can calculate the value of the gap. Formally, let us evaluate the FT of the k-th photocurrent, at the maximum of the reference target peak. Using equation (4.6) and equation (4.13),

$$Y_k(\tau_a) = \pi B_k R_a \exp\left[-j\xi\tfrac{\tau_a^2}{2} + j\omega_{0,k}\tau_a\right], \quad k = 1, 2. \tag{4.16}$$

The ratio of the two expressions in equation (4.16) yields the phase difference between the photocurrents:

$$\psi_a \equiv \frac{Y_1(\tau_a)}{Y_2(\tau_a)} = \exp\left[-j2\pi\tau_a(B+\delta)\right]. \tag{4.17}$$

Given the reference reflector delay τ_a and the frequency excursion B, the gap may be found using

$$\arg\left[\exp(j2\pi\tau_a B)\psi_a\right] = -2\pi\tau_a\delta. \tag{4.18}$$

The phase of a complex number can only be extracted modulo 2π, so that equation (4.18) can only be used to recover δ with an ambiguity of $1/\tau_a$. Therefore, the gap needs to be known to within $1/\tau_a$ before equation (4.18) may be applied. Using a

grating-based optical spectrum analyzer would yield the gap value with an accuracy of a few GHz, and we therefore need $1/\tau_a \gtrsim 10$ GHz. The nonzero linewidth of the source generates errors in the phase measurement ψ_a in equation (4.17) (see section 2.1.3.4). According to equation (4.18), the corresponding error in the gap calculation is inversely proportional to τ_a, and a large τ_a is therefore necessary to calculate δ accurately.

To overcome this issue, we use two reflectors τ_a and τ_b, and express the gap size as a function of the reflector separation. We define two phase factors

$$\psi_n \equiv \frac{Y_1(\tau_n)}{Y_2(\tau_n)}, \quad n = a, b \tag{4.19}$$

and calculate the two reflector-analog of equation (4.18):

$$\arg\left\{\exp\left[j2\pi(\tau_a - \tau_b)B\right]\frac{\psi_a}{\psi_b}\right\} = -2\pi(\tau_a - \tau_b)\delta. \tag{4.20}$$

From equation (4.20), $1/|\tau_a - \tau_b|$ can be chosen to be > 10 GHz to determine the value of δ. The error in this calculation is proportional to $1/|\tau_a - \tau_b|$. The accuracy of the gap calculation can now be improved by using equation (4.18), which yields a new value of δ with a lower error proportional to $1/\tau_a$. Depending on system noise levels, more stages of evaluation of δ using more than two reference reflectors may be utilized to achieve better accuracy in the calculations.

A potential MS-FMCW system architecture employing the stitching technique is shown in figure 4.6. The optical sources are multiplexed and used to image a target and a reference, as discussed above. The optical output is demultiplexed and measured using a set of photodetectors to generate the photocurrents of equation (4.13). The reference data is processed and used to stitch a target measurement with improved resolution. The multiplexing may be performed in time or optical frequency, or a combination of the two. The real power of the MS-FMCW technique then lies in its scalability. One envisions a system that combines cheap off-the-shelf SCLs to generate a swept-frequency ranging measurement that features an excellent

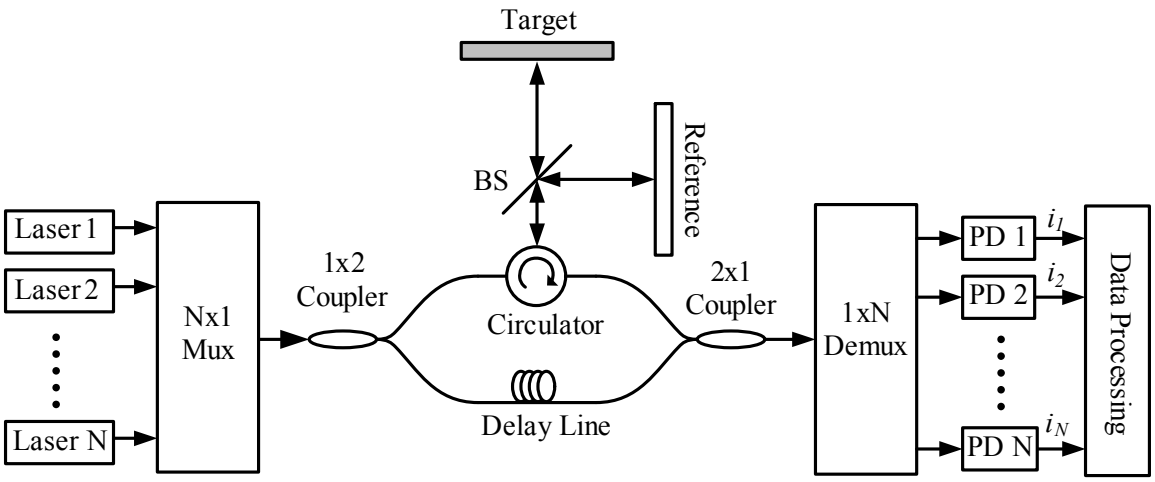

Figure 4.6: Proposed multiple source FMCW system architecture. BS: Beamsplitter. PD: Photodetector

combination of range resolution, scan speed, and imaging depth.

4.3 Experimental Demonstrations

4.3.1 Stitching of Temperature-Tuned DFB Laser Sweeps

Our first demonstration of the MS-FMCW technique was based on a 1550 nm DFB optoelectronic SFL (see chapter 3). The source generated a highly linear chirp with a bandwidth of 100 GHz and a scan time of 1 ms. We used the configuration of figure 4.5 with a two reflector reference characterized by $1/|\tau_a - \tau_b| \sim 10$ GHz (~ 3 cm free-space separation). This reference was chosen to accommodate the accuracy with which the gaps are initially known (~ 1 GHz). We tuned the SCL temperature through two set points to generate two 100 GHz sweeps with different starting frequencies. Optical spectra of the two sweeps (blue and red) are shown in figure 4.7. Even though it looks like the sweeps have significant overlap in optical frequency, the end of one is actually aligned to the beginning of the other. The perceived overlap is due to the nonzero width of the analyzer PSF, shown in black.

These sweeps were launched sequentially into the experiment, and the corresponding photocurrents were recorded. Applying the two-step procedure described in sec-

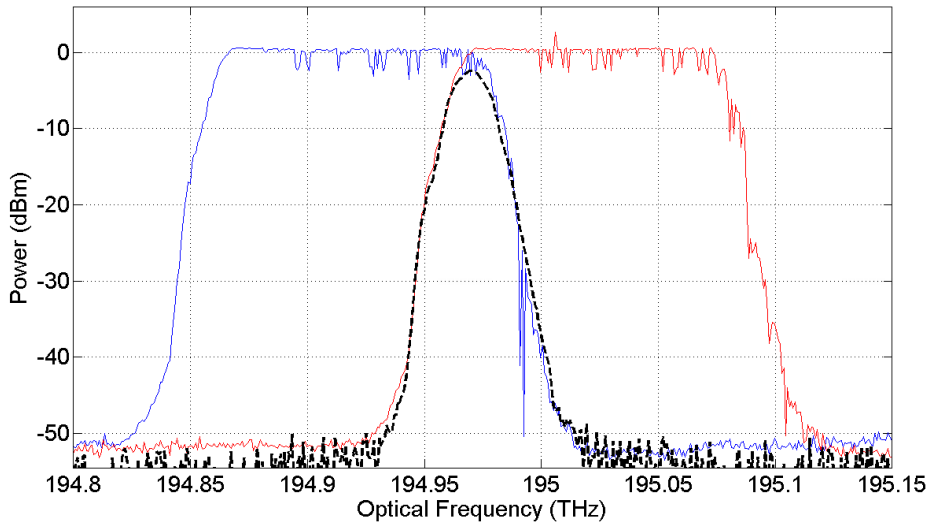

Figure 4.7: Optical spectra of the two DFB sweeps (blue and red) and the optical spectrum analyzer PSF (black)

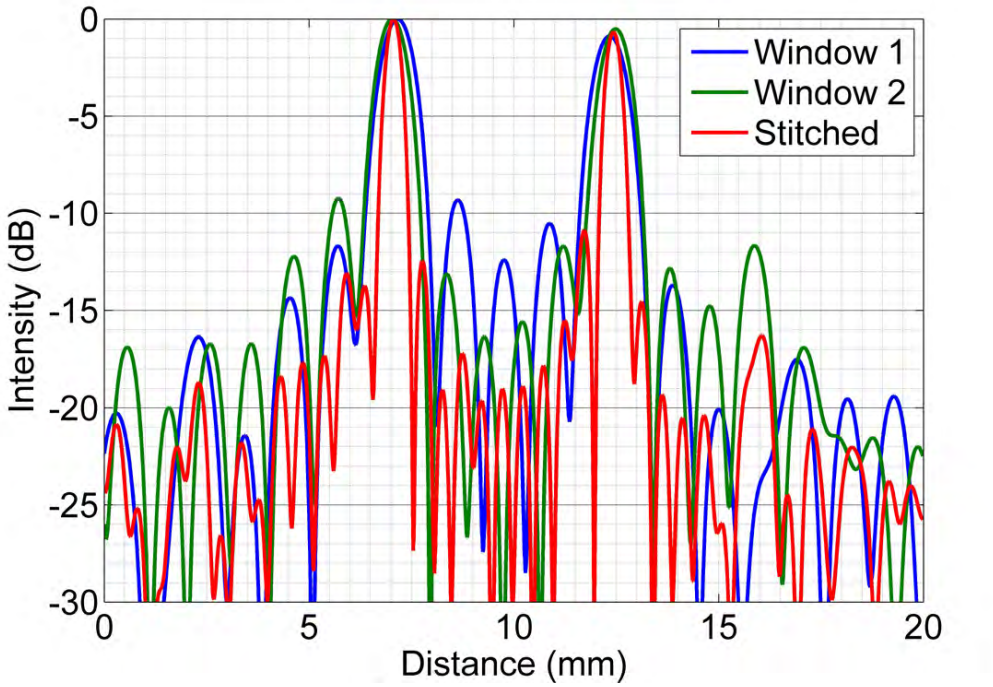

Figure 4.8: Single-sweep and stitched two-sweep photocurrent spectra of a dual reflector target with a separation of 5.44 mm. No apodization was used.

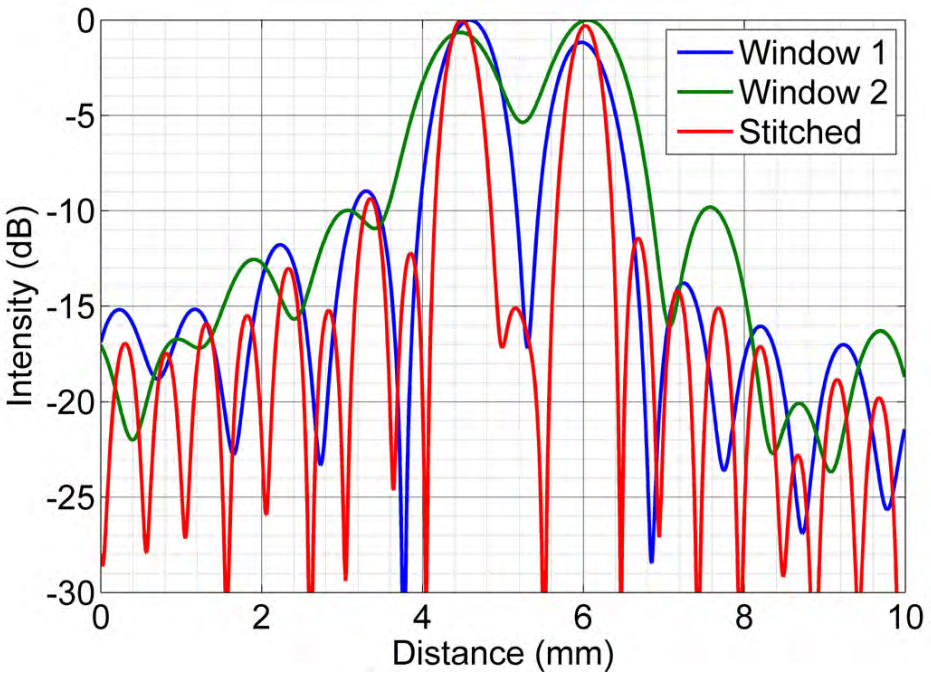

Figure 4.9: Single-sweep and stitched two-sweep photocurrent spectra of a dual reflector target with a separation of 1.49 mm. No apodization was used.

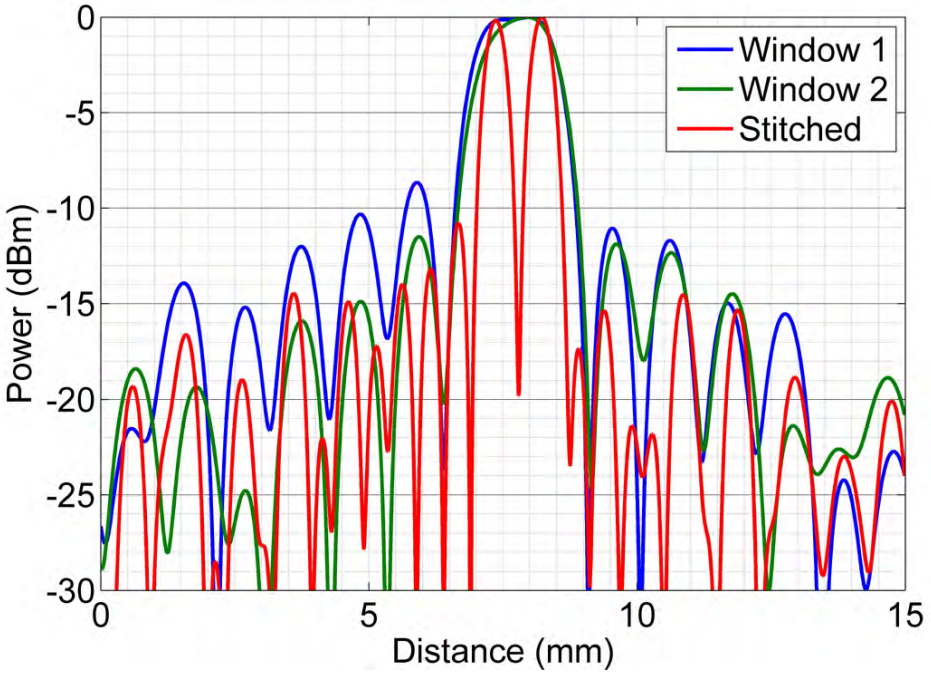

Figure 4.10: Single-sweep and stitched two-sweep photocurrent spectra of a dual reflector target with a separation of 1.00 mm (a microscope slide). No apodization was used.

tion 4.2.3, we recovered the gaps, and stitched the photocurrent spectra using equation (4.15). To characterize the range resolution of the system, we imaged slabs of transparent material (acrylic and glass). Reflections from the two slab interfaces were recorded for three slab thicknesses: 5.44 mm, 1.49 mm, and 1.00 mm (glass microscope slide). Figure 4.8, figure 4.9, and figure 4.10 show the ζ-domain photocurrent spectra for the three cases. The x-axis has been rescaled to correspond to distance in a material with refractive index 1.5, i.e., acrylic and glass. Each of the three figures shows the single-sweep spectra (blue and green), as well as the stitched spectrum (red). The FWHM of the peaks in the stitched plots is half of the FWHM of the peaks in the single-sweep plots, as predicted by equation (4.5). Figure 4.10 is of particular interest because the two peaks in the single-scan spectrum, corresponding to reflections from the two microscope slide facets, are barely resolved. This is consistent with the theoretical range resolution in glass of 1 mm for a 100 GHz sweep. The stitched curve shows two prominent peaks, demonstrating our improved ability to resolve two closely spaced targets.

By using more aggressive temperature and current tuning, we were able to extend the number of sweeps to three, and observe a threefold improvement in range resolution. The single-scan and stitched photocurrent spectra of a single reflector are shown in figure 4.11a. The single reflector spectra allows us to reliably measure the improvement in the FWHM of the axial PSF. The FWHMs are 12.17 ps and 4.05 ps for the single and multiple source cases, respectively. Using equation (4.5) we calculate the free-space range resolutions to be 1.51 mm and 500 μm. The threefold range resolution enhancement is consistent with equation (4.12). The improvement in resolution again allows us to resolve the two reflections from the 1 mm glass microscope slide in figure 4.11b. The measured peak separation of 10 ps is the round-trip delay between the two slide facets, and indeed corresponds to a glass thickness of 1 mm.

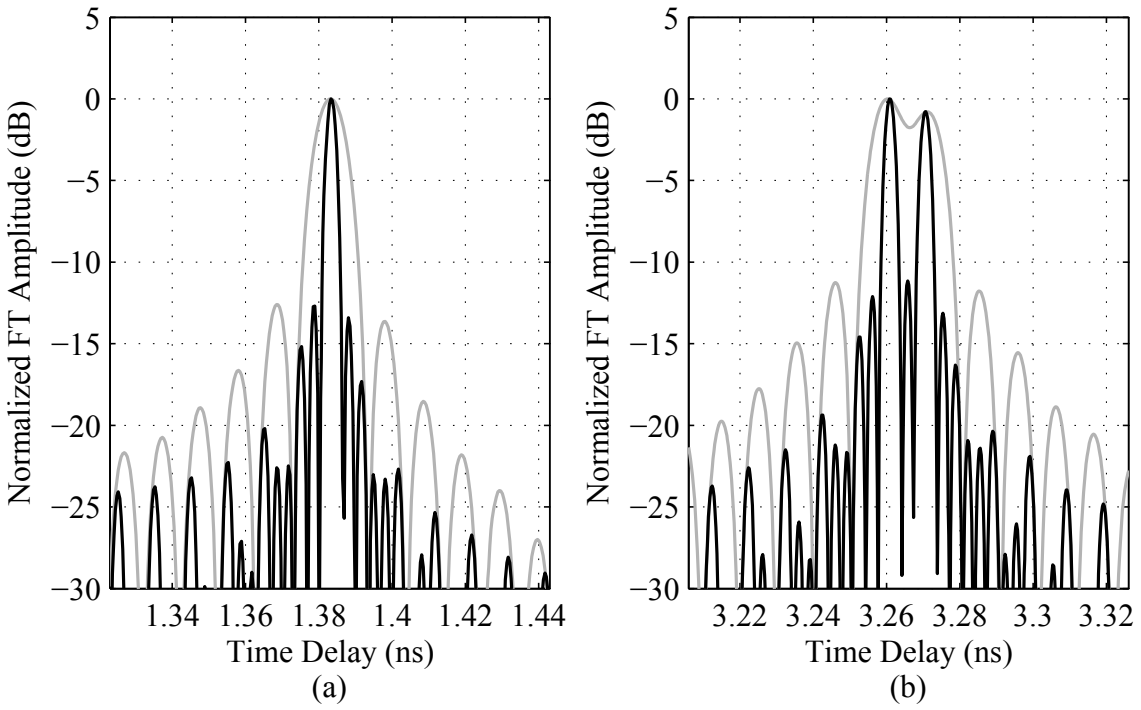

Figure 4.11: The gray and black curves correspond to single-sweep and stitched three-sweep photocurrent spectra, respectively. No apodization was used. (a) Single reflector spectrum. (b) Glass slide spectrum. The peaks correspond to reflections from the two air-glass interfaces. The slide thickness is 1 mm.

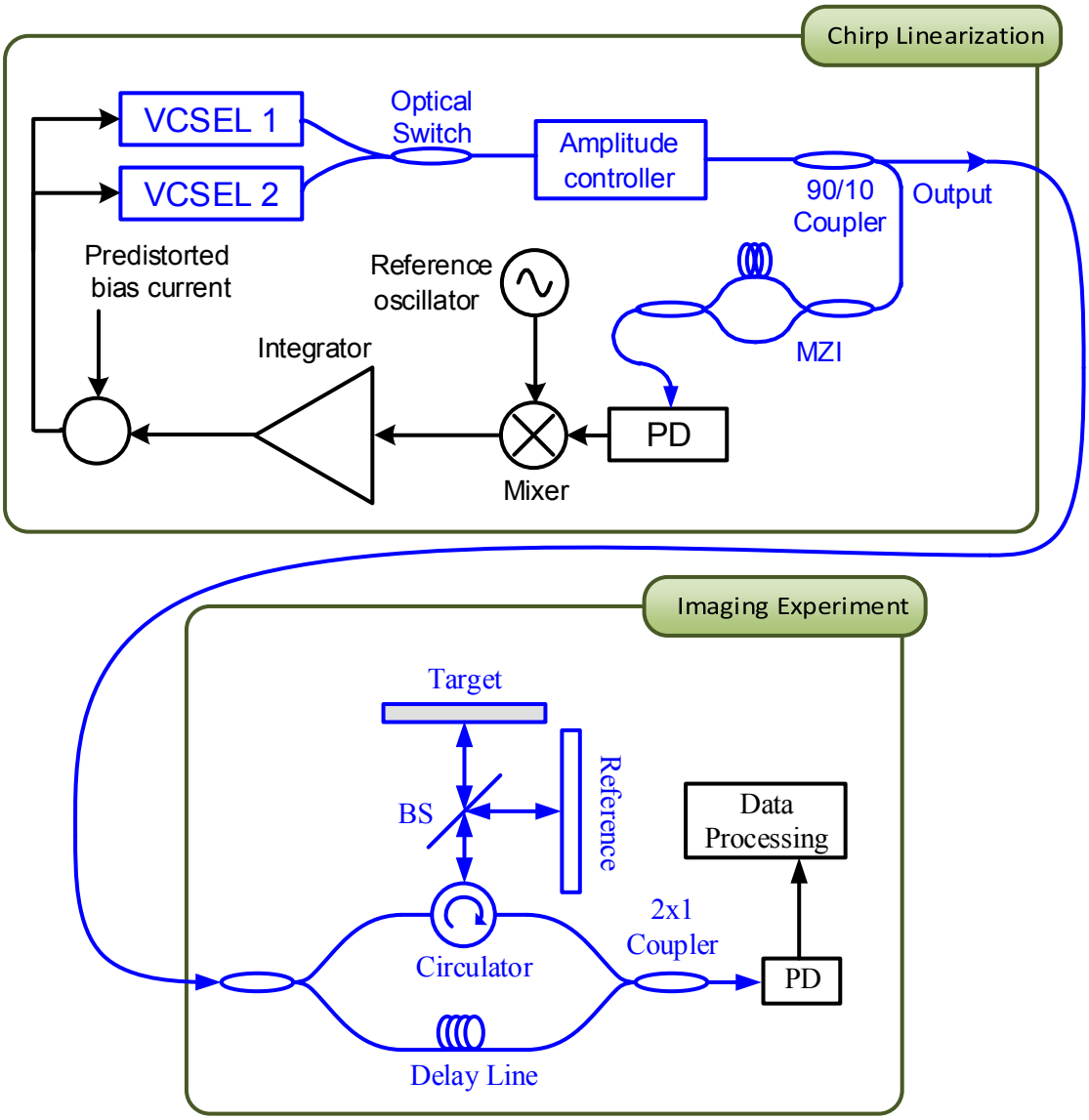

Figure 4.12: Dual VCSEL FMCW reflectometry system diagram. The feedback loop ensures chirp stability. A reference target is used to extract the inter-sweep gaps. PD: Photodiode, BS: Beamsplitter

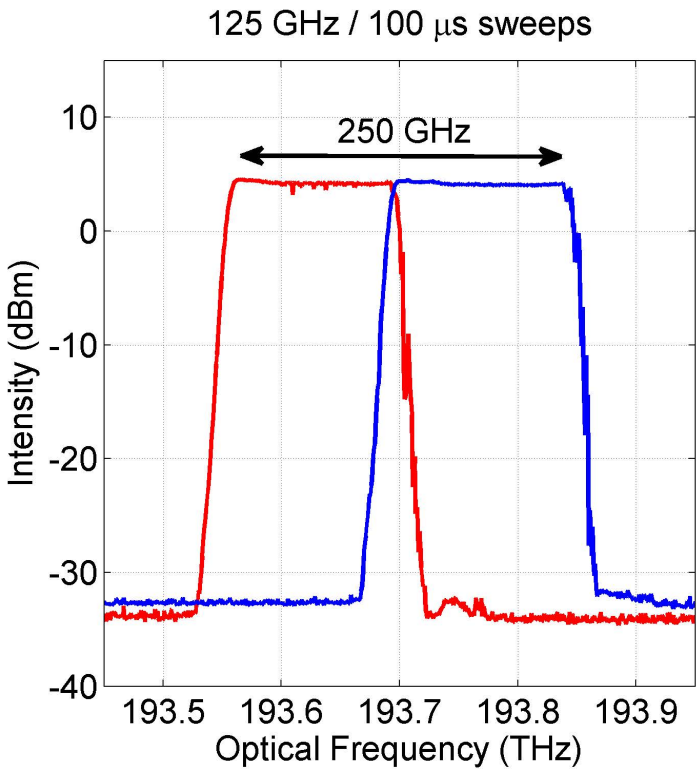

Figure 4.13: Optical spectra of the two VCSEL sweeps in the 250 GHz experiment

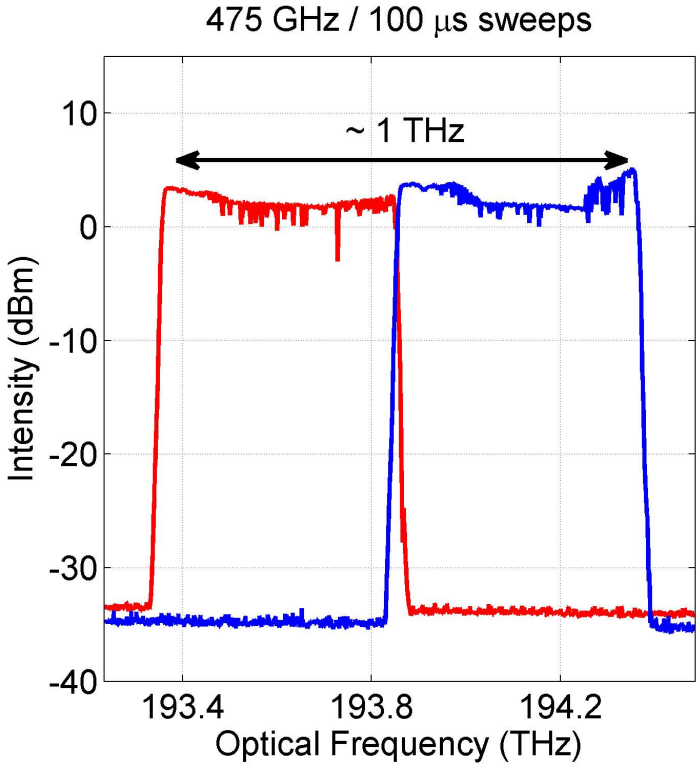

Figure 4.14: Optical spectra of the two VCSEL sweeps in the ~ 1 THz experiment

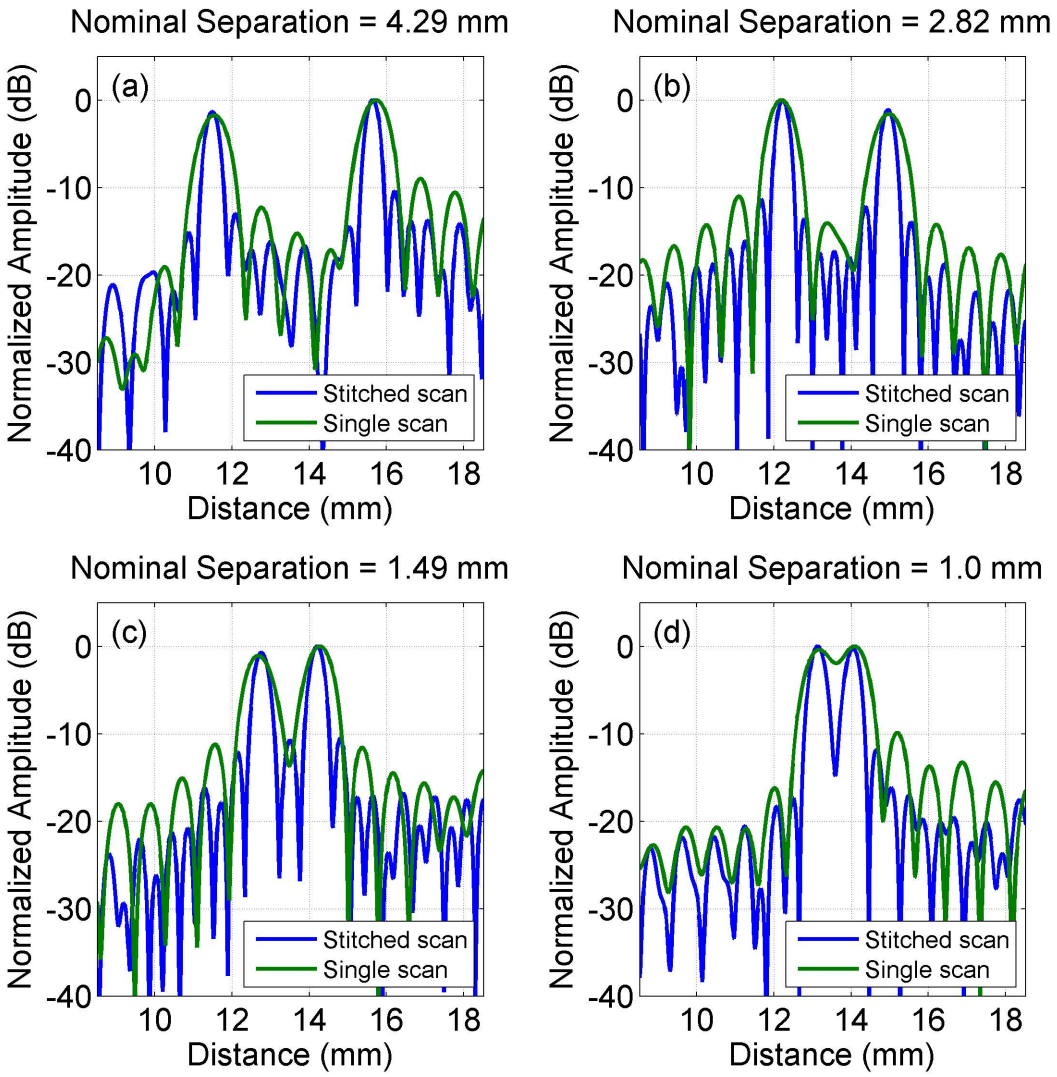

Figure 4.15: Single-sweep and stitched two-sweep photocurrent spectra of dual reflector targets with various separations. The total chirp bandwidth is 250 GHz. No apodization was used.

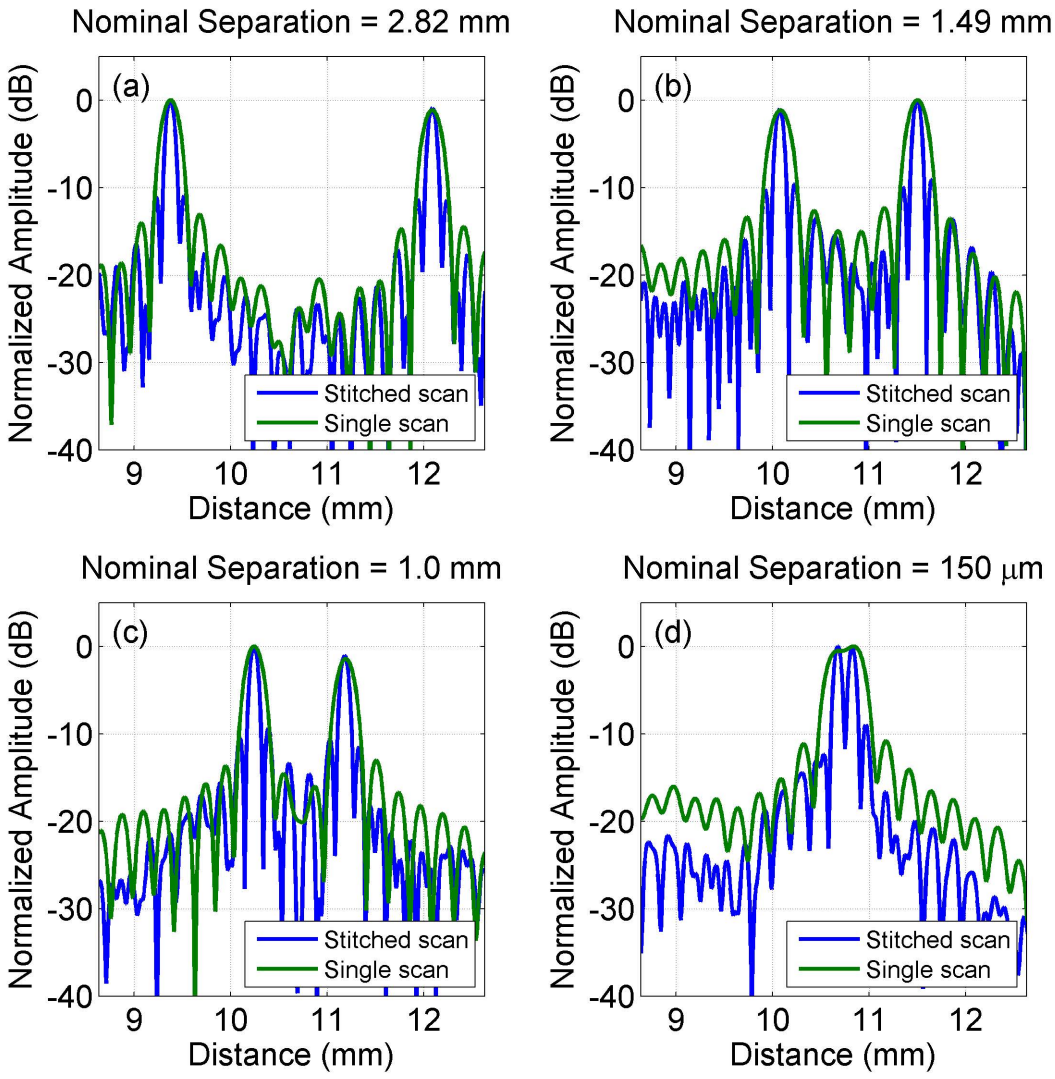

Figure 4.16: Single-sweep and stitched two-sweep photocurrent spectra of dual reflector targets with various separations. The total chirp bandwidth is ~ 1 THz. No apodization was used.

4.3.2 Stitching of Two VCSELs

In the current section we describe the next phase of our MS-FMCW experiments—the stitching of two commercial VCSELs at 1550 nm. When compared to DFB lasers, VCSELs offer increased tunability, a faster chirp rate, as well as a significant cost reduction (see section 3.3.1).

In the proof-of-principle DFB experiment we used a single laser and tuned its temperature through multiple setpoints to generate up to three sweeps. The SCL temperatures needed to equilibrate before data collection, and as a result, the system scan time was about ten minutes. In this experiment, we used two VCSELs and an optomechanical switch in a feedback loop to form an optoelectronic SFL, as shown in figure 4.12. The switch selects a particular VCSEL, and the feedback imposes a perfectly linear chirp. Each VCSEL completed its chirp in 100 μs, but the total scan time was limited by the switch to about 20 ms.

We started our experiment with conservative tuning of 125 GHz per channel. The temperatures of the VCSELs were tuned to align their optical spectra to each other, as shown in figure 4.13. As before, we included a reference target to aid in the gap recovery procedure. Figure 4.15 compares single-source and stitched axial scans of acrylic and glass slabs of varying thicknesses. As expected, the stitched scans have a higher axial resolution, as evidenced by both the reduced FWHM of the axial PSF, as well as our ability to resolve the surfaces of the 1 mm glass slide in figure 4.15d.

We continued our experiment with more aggressive temperature and current tuning, which yielded 475 GHz of optical bandwidth per channel, with a total chirp bandwidth of just under 1 THz, as shown in figure 4.14. This bandwidth corresponds to a free-space axial resolution of $\sim$ 150 μm, and a glass resolution of $\sim$ 100 μm. Two-target axial scans are shown in figure 4.16. As before, stitching the photocurrents narrowed the axial PSF. The thinnest target we used was a glass microscope coverslip with a nominal thickness of 150 μm, which showed up as a single broad peak in the single sweep, but was resolved into two reflections in the stitched scan.

4.3.3 Hardware Stitching of Four VCSELs

Previous stitching experiments relied on a simultaneous measurement of a multi-reflector reference target to determine the inter-sweep gaps. Our next stitching experiment relied on the optoelectronic SFL to control the starting sweep frequencies of each channel. We used four 1550 nm VCSEL-based optoelectronic SFLs in the configuration of figure 4.17. The electric fields of each channel were added using a 4×1 fiber coupler. Each VCSEL was chirped 500 GHz in 100 μs, and then turned off. We allocated 25 μs between adjacent channel time slots to allow the previous laser to turn off, and the next laser to turn on. The total scan time was therefore 500 μs.

As described in section 3.2.2, locked states of the optoelectronic SFL form a family of linear chirps, separated by the loop MZI FSR in optical frequency. These locked states are shown schematically in red in figure 4.19. A locked SFL (shown in black) aligns itself to the state that most closely matches its free-running chirp. Tuning the SCL temperature and initial sweep current can therefore be used to shift the SFL to a particular locked state. We used an MZI with a relatively large FSR of 9.6 GHz to lock the VCSELs. As a result, the SFLs locked to the same state from scan to scan, generating precisely repeatable linear chirps. Moreover, because the SFLs used the same MZI, it was possible to tune all four channels to the same locked state, as shown in the blue curve in figure 4.19.

The combination of repeatable chirps and the ability to lock the SFLs to the same chirped state obviates the gap recovery procedure that was necessary in previous iterations of our MS-FMCW systems. The stitching is therefore essentially performed by the SFL hardware, which enables real-time processing of the MS-FMCW photocurrents. We used a coarse 80.2 GHz FSR MZI to tune the SCL temperatures and ensure that the SFLs are locked to the same chirped state. This MZI was used purely for calibration at start-up, and the acquisition of the coarse MZI signal was not necessary to process the MS-FMCW measurement.

Each channel in the hardware stitching system generated a 500 GHz sweep, for a total chirp bandwidth of 2 THz, as shown in figure 4.18. This corresponds to a

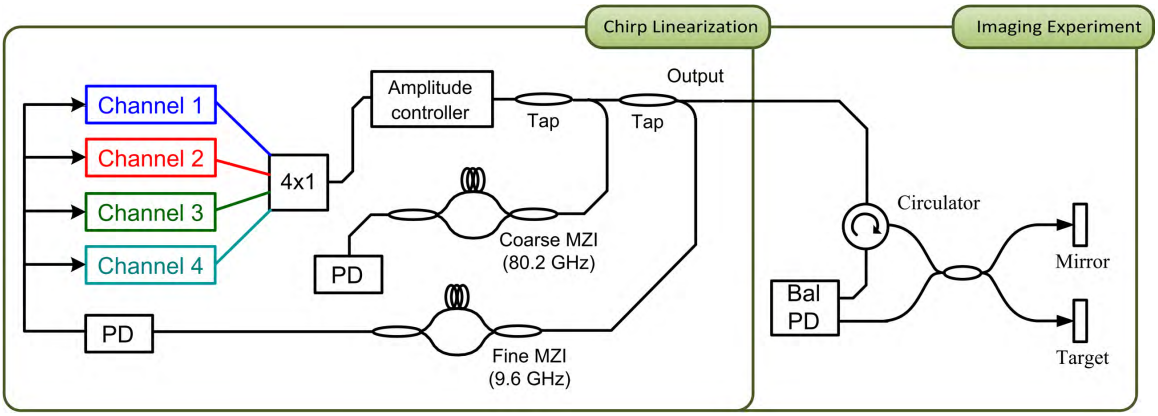

Figure 4.17: Four channel 2 THz hardware stitching experiment

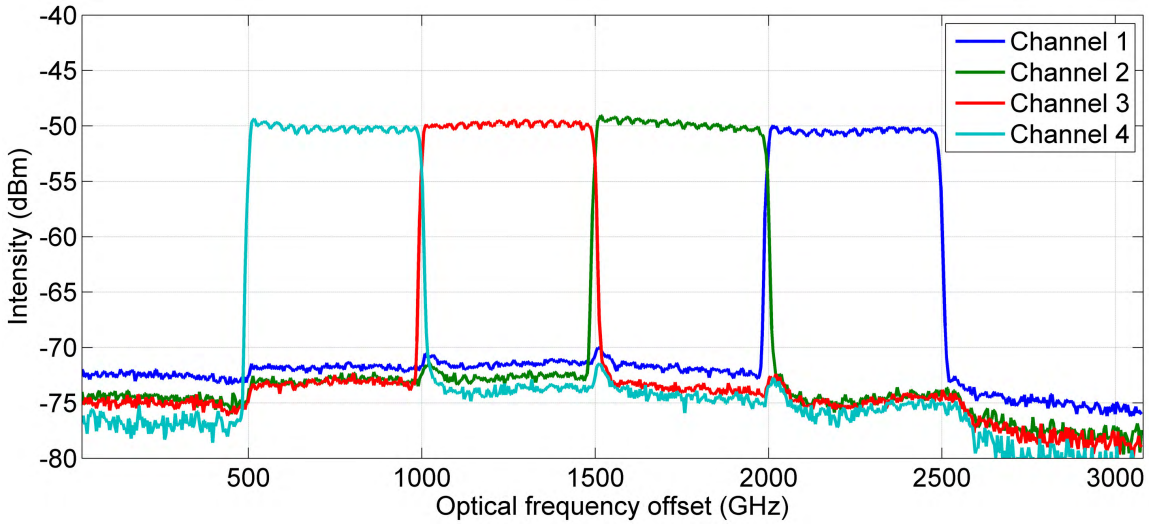

Figure 4.18: Optical spectra of the four 1550 nm VCSEL sweeps in the 2 THz hardware stitching experiment

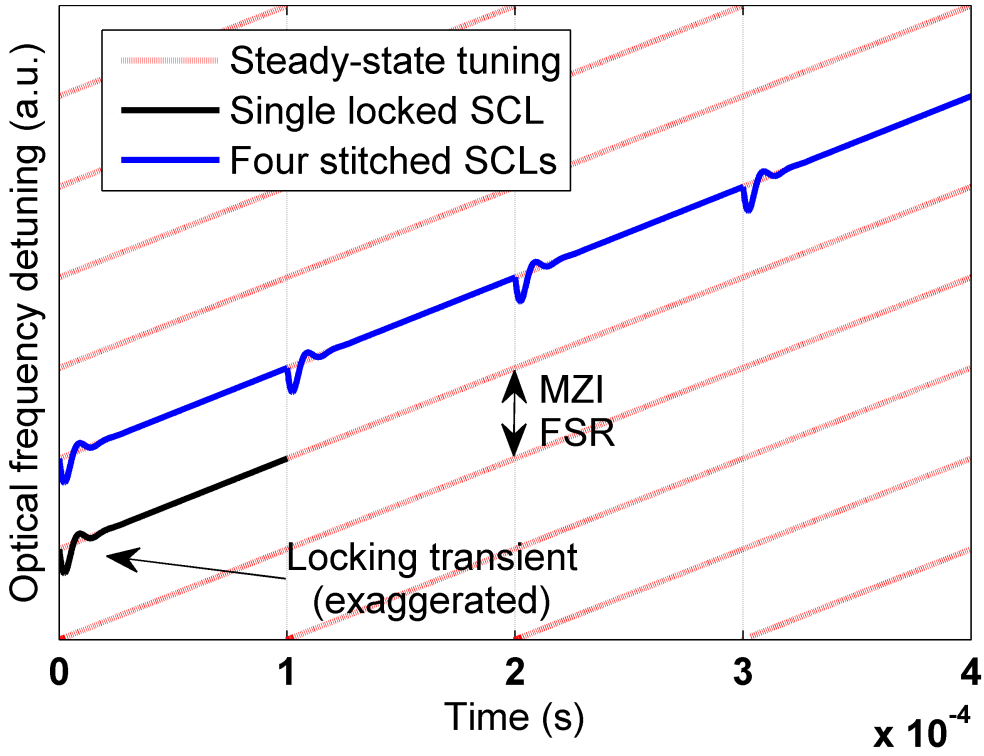

Figure 4.19: Schematic representation of a family of locked states (red) of the opto-electronic SFL. In lock, the SCL (black) follows the locked state that most closely matches its free-running chirp. In hardware stitching, temperatures and currents are tuned so that all the MS-FMCW channels operate in the same locked state (blue).

range resolution of 75 μm in free space, and 50 μm in glass. We imaged a 150 μm glass microscope coverslip that was suspended above a metal surface. The time-domain stitched photocurrent is shown in the top panel of figure 4.20. The curve was generated by measuring the photocurrent during each channel's time slot, and appending the four data sets to each other. The SFL hardware enables perfect real-time stitching, and we therefore observe a continuous time-domain curve. Single-sweep (black) and stitched (red) photocurrent spectra are shown in the bottom panel of figure 4.20. The x-axis is scaled to correspond to distance in glass. The time-domain photocurrents were apodized with a Hamming window before calculating the FT. The windowing suppressed the sinc sidebands seen in previously calculated photocurrent spectra, at the cost of broadening the PSF by a factor of 1.37. The Hamming-broadened glass resolutions are therefore 274 μm for the single-sweep, and 68.5 μm for the stitched measurement.

In the single-sweep photocurrent spectrum we observe two broad peaks, one due to reflections from the coverslip, and the other one due to a reflection from the metal surface underneath. In the stitched spectrum, the front and back coverslip surfaces are perfectly resolved, and the peak due to the metal surface is narrowed by a factor of four.

4.4 Summary

We have analyzed and demonstrated a novel variant of the FMCW optical imaging technique. This method combines multiple lasers that sweep over distinct but adjacent regions of the optical spectrum, in order to record a measurement with increased effective optical bandwidth and a corresponding improvement in the range resolution. The MS-FMCW technique is highly scalable and is a promising approach to realize a wide-bandwidth swept-frequency imaging system that inherits the speed and coherence of the SCL.

We have described the various phases of our experimental work on MS-FMCW. We started with a single DFB proof-of-concept experiment that relied on temperature tuning to generate three sweeps of 100 GHz each, for a total chirped bandwidth of 300 GHz. Because the laser temperature had to equilibrate between sweeps, the system scan time was about 10 minutes. We then moved on to a two-source VCSEL-based system with a bandwidth of 500 GHz per channel, and a total chirp bandwidth of 1 THz. We used an optomechanical switch to select the particular VCSEL channel, which limited the minimum scan time to about 20 ms. The last MS-FMCW iteration took advantage of the starting frequency control of the optoelectronic SFL to essentially perform real-time stitching in hardware. We used four VCSEL channels, and turned them on one at a time. Each VCSEL chirped 500 GHz in 100 μs, with a total chirp bandwidth of 2 THz and a scan time of 500 μs.

These results demonstrate the possibility of high-resolution depth imaging, e.g., optical coherence tomography, in a SCL-based platform with no moving parts.

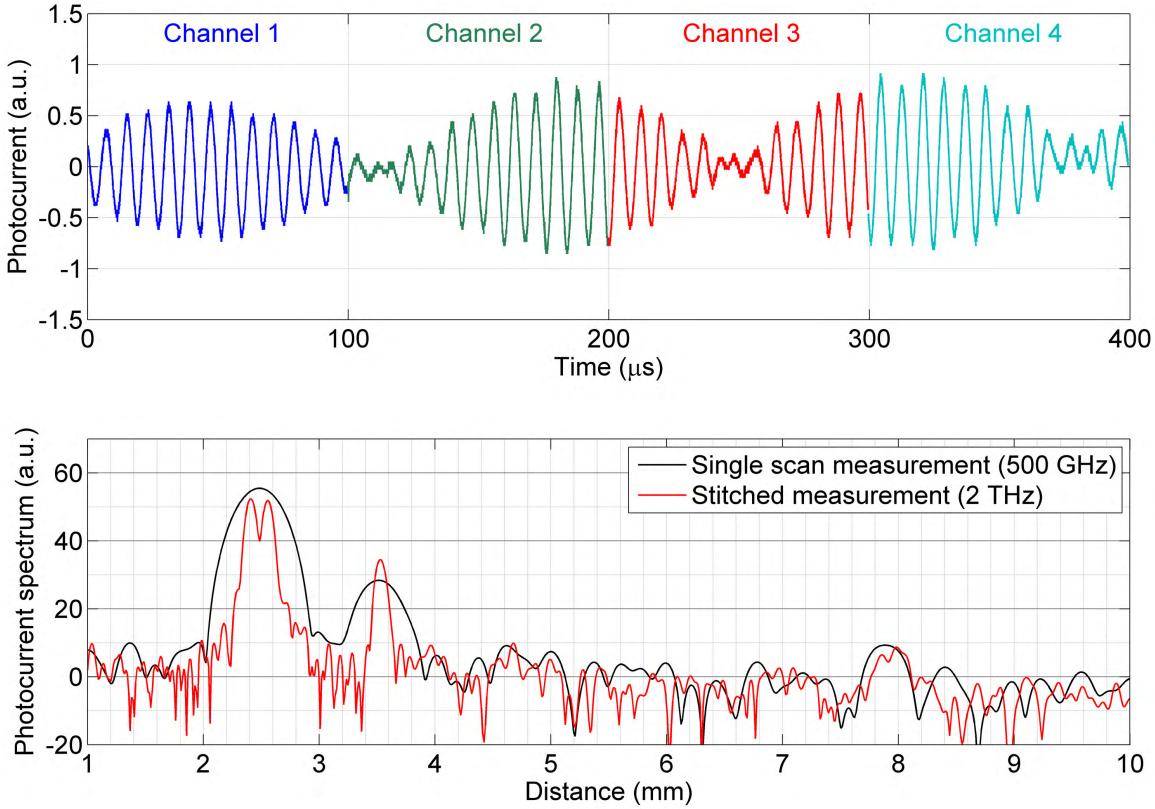

Figure 4.20: Top panel: time-domain stitched photocurrent in the hardware stitching experiment. Bottom panel: Single-sweep (black) and stitched four-sweep (red) photocurrent spectra of a 150 μm glass microscope coverslip suspended above a metal surface. The spectra are apodized with a Hamming window. The total chirp bandwidth is 2 THz.